Z. Kristallogr. **2013**, *228*, 28–34 / **DOI** 10.1524/zkri.2013.1556

Layered oxygen vacancy ordering in Nb-doped $SrCo_{1-x}Fe_xO_{3-\delta}$ perovskite

Senne Van Rompaey[I], Walid Dachraoui[I], Stuart Turner[I], Olga Yu. Podyacheva[II], Haiyan Tan[I], Jo Verbeeck[I], Artem Abakumov[I] and Joke Hadermann*,[I]

[I] EMAT, University of Antwerp, Groenenborgerlaan 171, 2020 Antwerp, Belgium
[II] Boreskov Institute of Catalysis, Novosibirsk 630090, Russia

Dedicated to Professor Sven Hovmöller on the occasion of his 65th birthday

Received July 8, 2012; accepted August 27, 2012
Published online: October 22, 2012

Solid oxide fuel cell / Perovskite / TEM / PED / Mixed ionic-electronic conductor

Abstract. The crystal structure of $SrCo_{0.7}Fe_{0.2}Nb_{0.1}O_{2.72}$ was determined using a combination of precession electron diffraction (PED), high-angle annular dark field scanning transmission electron microscopy (HAADF-STEM) and spatially resolved electron energy loss spectroscopy (STEM-EELS). The structure has a tetragonal *P*4/*mmm* symmetry with cell parameters $a = b = a_p$, $c = 2a_p$ (a_p being the cell parameter of the perovskite parent structure). Octahedral BO_2 layers alternate with the anion-deficient $BO_{1.4}$ layers, the different B cations are randomly distributed over both layers. The specific feature of the $SrCo_{0.7}Fe_{0.2}Nb_{0.1}O_{2.72}$ microstructure is a presence of extensive nanoscale twinning resulting in domains with alignment of the tetragonal *c*-axis along all three cubic direction of the perovskite subcell.

1. Introduction

Complex oxide $SrCo_{1-x}Fe_xO_{3-\delta}$ is a mixed ionic-electronic conductor, with a cubic perovskite structure at ambient conditions [1]. Mixed ionic-electronic conductors can be used as membranes for separating oxygen from other gasses and as cathodes in solid oxide fuel cells. $SrCo_{0.8}Fe_{0.2}O_{3-\delta}$ was found to possess the highest oxygen flux in the series of the $La_{1-x}Sr_xCo_{1-y}Fe_yO_{3-\delta}$ perovskites [1]. However, this perovskite suffers from limited stability in a reducing environment. Increasing the concentration of oxygen vacancies causes these to order, which has a negative effect on the oxygen mobility and introduces unwanted mechanical stress [2, 3]. Below 770 °C $SrCo_{0.8}Fe_{0.2}O_{3-\delta}$ adopts the oxygen vacancy ordered brownmillerite structure at $p(O_2) \sim 10^{-4}$ atm, whereas at higher $p(O_2) \sim 0.04$ atm perovskite and brownmillerite form a two-phase mixture [4]. Above 770–790 °C $SrCo_{0.8}Fe_{0.2}O_{3-\delta}$ transforms into a disordered perovskite structure resulting in an abrupt change in the activation energy of its oxygen permeation flux [5, 6]. The high temperature disordered perovskite structure can be stabilized at room temperature by Nb doping. Lu *et al.* reported an oxygen permeation flux for the $SrCo_{0.8}Fe_{0.1}Nb_{0.1}O_{3-\delta}$ membrane of 1.80 ml min^{-1} cm^{-2} under an air/helium gradient at 950 °C and good oxygen permeation stability. [7] This oxygen permeation flux is indeed higher than that found under the same circumstances for membranes of $SrCo_{0.8}Fe_{0.2}O_{3-\delta}$ and $Ba_{0.5}Sr_{0.5}Co_{0.8}Fe_{0.2}O_{3-\delta}$, resp. 1.60 and 1.25 ml min^{-1} cm^{-2} [8, 9]. The $SrCo_{0.8-x}Fe_{0.2}Nb_xO_{3-\delta}$ solid solutions ($x = 0.2$) preserve the cubic perovskite structure up to 1000 °C upon heating in air or in vacuum (10^{-5} atm) [10], whereas the samples with $x = 0.1$ and 0.3 demonstrate peak-splitting indicating structural changes. However, a more detailed investigation with synchrotron X-ray powder diffraction revealed that the $x = 0.1$, 0.2 samples lose oxygen starting from $T \sim 400$ °C, decomposing into two perovskite phases with close lattice parameters [11]. No more detailed information is available at the moment on the composition and structure of these phases, or on the nature of the transformation.

In this contribution we fill the gap in knowledge of the exact structure of the $SrCo_{0.8-x}Fe_{0.2}Nb_xO_{3-\delta}$ solid solutions. Using a combination of transmission electron microscopy techniques we demonstrate that the crystal structure of $SrCo_{0.7}Fe_{0.2}Nb_{0.1}O_{2.72}$ at room temperature is far from being disordered cubic perovskite, but is built up of nanotwinned domains with layered ordering of oxygen atoms and vacancies.

2. Experimental

The sample with nominal composition $SrCo_{0.7}Fe_{0.2}Nb_{0.1}O_{3-\delta}$ was synthesized according to the procedure described earlier [10]. The composition was verified using energy dispersive X-ray (EDX) analysis on 50 different crystallites, performed with a JEOL JSM5510 scanning electron microscope with EDX attachment (Oxford INCA System). The oxygen non-stoichiometry (δ) in $SrCo_{0.7}Fe_{0.2}Nb_{0.1}O_{3-\delta}$ was determined

* Correspondence author (e-mail: joke.hadermann@ua.ac.be)

by the use of standard iodometric titration [12, 13]. The samples for the transmission electron microscopy (TEM) studies were prepared by crushing the powder in ethanol and dispensing some drops of the solution on a copper grid covered by a holey-carbon film. Selected area electron diffraction (SAED) and precession electron diffraction (PED) patterns were obtained using a Philips CM20 transmission electron microscope with a LaB_6 filament operating at an acceleration voltage of 200 kV, equipped with a Spinning Star precession attachment. The PED and SAED patterns were recorded using a CCD camera. All PED patterns were recorded with a precession angle of 2.5°. The integrated intensities of the reflections were extracted using the original software IDEA. IDEA uses the following procedure for extracting the integrated intensity of the reflections in a PED pattern: the background is estimated by taking three distinct line profiles of the PED pattern running through the central beam. This forms a dataset of points (d, I) with d the distance to the central beam and I the intensity at this distance. To this dataset, a one dimensional function B is fitted in an iterative way to estimate the background at a distance d to the central beam, $B = a_1 \cdot (a_2 \cdot |d|^{a_3} + (1 - a_2) \cdot e^{-|d|^{a_4}}) + a_5$, where a_i ($i = 1 : 5$) are the fittable parameters. A lattice is constructed corresponding to all reflections present on the PED pattern. To each reflection a 2D pseudo-Voigt function is fitted while taking the estimated background into account. The fitted function is then numerically integrated between elliptical boundaries depending on the FWHM of the pseudo-Voigt fit. The structure refinement was performed with JANA2006 [14].

High angle annular dark field scanning transmission electron microscopy (HAADF-STEM) images were obtained using a Tecnai G^2 transmission electron microscope operating at 200 kV. Simulated HAADF-STEM images were made with QSTEM [15]. HR-HAADF-STEM and STEM-EELS experiments were carried out on a FEI Titan 80–300 "cubed" microscope fitted with an aberration-corrector for the probe forming lens and a monochromator, operated at 120 kV. The STEM convergence semi-angle used was ~20 mrad. For HAADF-STEM imaging (Fig. 3a), an inner collection semi-angle β of 85 mrad was used. Spectroscopy experiments were performed on a GIF-QUANTUM spectrometer, acquiring simultaneous ADF and EELS signals. The EELS collection semi-angle β and inner ADF detection angle during the spectroscopy experiments was ~100 mrad. To generate the atomic resolution elemental maps, the acquired EELS data was PCA treated and reconstructed using 3 principal components. After reconstruction, the EELS edges were background subtracted, and maps generated using appropriate integration windows. The high resolution EELS data (Fig. 3d, e) was acquired in STEM mode with the monochromator excited to provide an energy resolution of 250 meV. The STEM convergence semi-angle used was ~20 mrad, the collection angle was ~60 mrad.

3. Results

The cation composition of the compound was found with EDX analysis to be $Sr_{1.08(8)}Co_{0.65(8)}Fe_{0.20(3)}Nb_{0.15(4)}O_{3-\delta}$, in agreement with the nominal composition $SrCo_{0.7}Fe_{0.2}Nb_{0.1}O_{3-\delta}$. The measured cation composition does not deviate from the nominal composition of the sample by more than two standard deviations. The oxygen content measured with the iodometric titration corresponds to $\delta = 0.28$, so that the nominal composition $SrCo_{0.7}Fe_{0.2}Nb_{0.1}O_{2.72}$ was adopted. Series of SAED patterns were recorded from a large number of crystallites of $SrCo_{0.7}Fe_{0.2}Nb_{0.1}O_{2.72}$. Figure 1 shows representative patterns (top row) indexed in the parent cubic perovskite cell with $a_p = 3.885(5)$ Å [10]. However, extra reflections are present which cannot be indexed using the cubic cell. All SAED patterns can be indexed using a tetragonal unit cell with the lattice parameters $a = a_p = 3.885$ Å, $c = 2a_p = 7.77$ Å, when taking into account the presence of twinning. The indexation in the tetragonal supercell is shown on the schematic representation at the bottom of Fig. 1. More SAED patterns, taken in PED mode, can be found in the Supporting Information. No reflections conditions were observed, suggesting *P4/mmm* as the most symmetric space group.

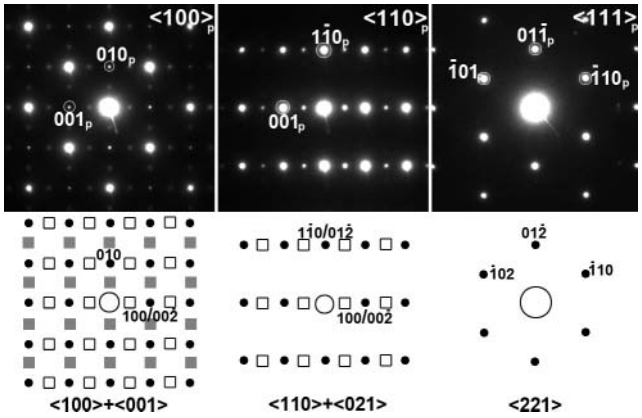

Fig. 1. Representative electron diffraction patterns of $SrCo_{0.7}Fe_{0.2}Nb_{0.1}O_{2.72}$ with the subcell reflections indexed using the parent perovskite cell parameters a_p (top row, experimental patterns) and indexed using the new tetragonal cell (bottom row, schematic patterns). The indices on the schemes belong with the nearest black dot. Black dots represent reflections present in all overlapping patterns, open squares in the first pattern are reflections only present in the ⟨100⟩ zones, grey filled squares are present in the ⟨100⟩ zones after a rotation over 90° around the zonal axis, only the black dots are present in ⟨001⟩. In the second pattern open squares are only present in the ⟨110⟩ zones, in the ⟨021⟩ zones only the black dots are present.

The nano-sized twinned domains of the tetragonal structure are visualized in the HAADF-STEM image along [100] (Fig. 2). A HAADF-STEM image shows dots corresponding to the projected atomic columns, with the brightness of the dot being related to the average Z over the whole projected column. On this image a clear doubling of the periodicity occurs along one of the perovskite axes, which becomes the c-axis of the tetragonal supercell. In the left top part of Fig. 2 the c-axis is horizontally oriented, while in the bottom left and top right part the c-axis is directed vertically. The brightest dots in the image correspond to the Sr cations ($Z = 38$; compared to Fe, Co and a minority of Nb with $Z = 26$, 27 and 41, respectively). The alternation of dark contrast occurs in-between two consecutive SrO layers at the $BO_{2-\delta}$ layers, indicating that two subsequent B–O layers are not anymore equiva-

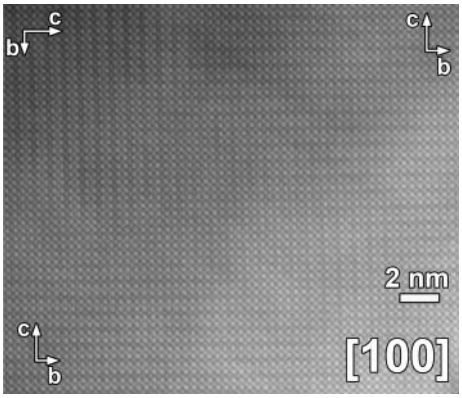

Fig. 2. HAADF-STEM image of $SrCo_{0.7}Fe_{0.2}Nb_{0.1}O_{2.72}$.

lent due to either B-cation ordering and/or ordering of oxygen atoms and vacancies. It should be noted that the HAADF-STEM image in Fig. 2 shows striking similarity to the HAADF-STEM images of the anion-deficient perovskites (La, Sr)$FeO_{3-\delta}$ and $SrCoO_{3-\delta}$, where layered ordering of oxygen atoms and vacancies was also detected. [16, 17].

To shed light on a possible cation ordering as the origin of the contrast variations in the HAADF-STEM images, atomic resolution elemental maps were acquired using spatially resolved electron energy-loss spectroscopy (STEM-EELS). The results are displayed in Fig. 3. To acquire the atomic resolution elemental maps, the so-called spectrum imaging technique (SI) was adopted [18]. In this technique, the Angstrom-sized electron probe used in aberration-corrected STEM is scanned over the sample, and an EELS spectrum and ADF signal is acquired in each point. To this end, a $22 \cdot 33$ pixel SI was acquired from a region similar to the one indicated in Fig. 3a. The ADF signal acquired together with the EELS data confirms that the SI contains dark and light-contrast layers. Elemental maps were generated from the acquired EELS data (see experimental section) and are plotted in Fig. 3b. The elemental maps show that Nb, Fe and Co are all present at all B cation positions. No preferential enrichment of the elements can be made out at a light- or dark-contrast layer. All A cation positions are logically Sr. As no preferential enrichment of the B cation elements could be made out in the light- or dark-contrast layers, the contrast change in the B−O layers is most likely due to ordering of the oxygen vacancies and not to the order of cations in the B positions.

Summed EELS data from a light and dark layer, containing the Fe $L_{2,3}$ and Co $L_{2,3}$, are plotted in Fig. 3c. For transition metals, the fine structure of the $L_{2,3}$ edges is known to be sensitive to both valency and coordination [19]. Visual inspection of the Co and Fe edges reveals no major changes in EELS fine structure, ruling out any valency changes of Fe and Co over the layers. The subtle changes associated with coordination cannot be picked up at the energy resolution used for these experiments (approximately 1.1 eV) [20]. By comparing the fine structure and energy onset of the Fe $L_{2,3}$ and Co $L_{2,3}$ edges to standards, the valency of Fe and Co were determined. To maximise the fine structure in the EELS spectra, the two edges were acquired from the bulk sample, using an excited monochromator providing an energy resolution of

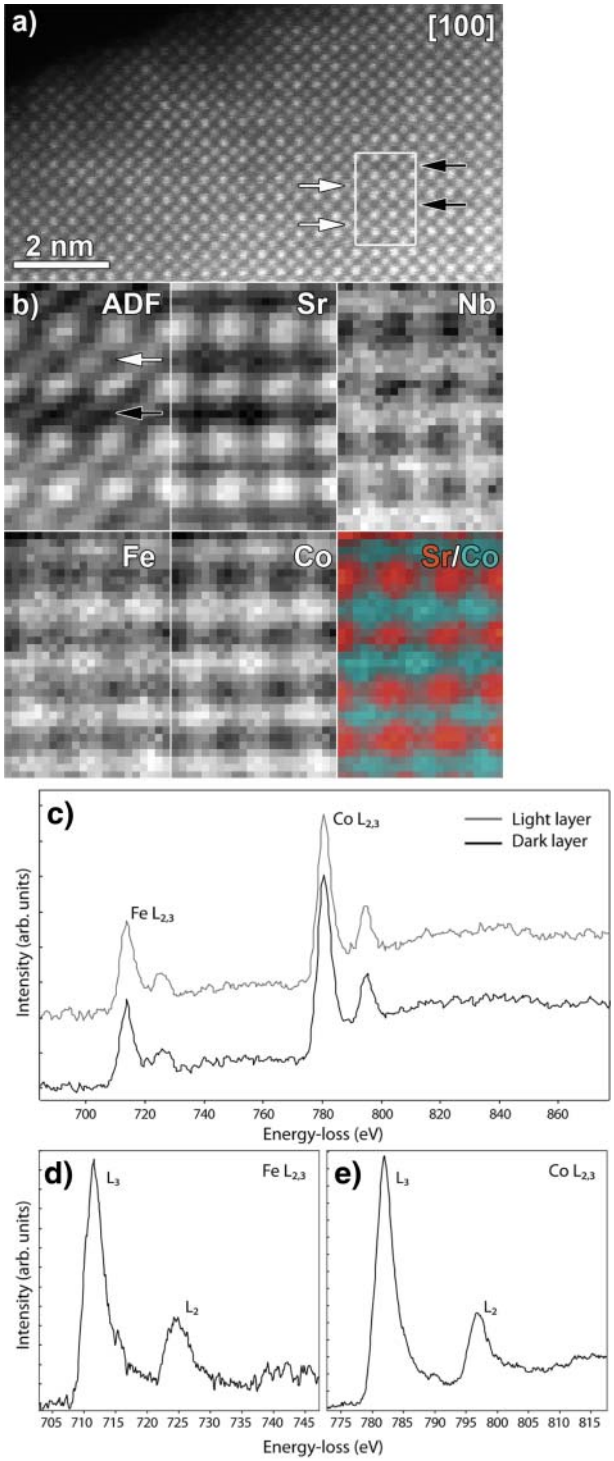

Fig. 3. STEM-EELS elemental mapping of sample $SrCo_{0.7}Fe_{0.2}Nb_{0.1}O_{2.72}$ and monochromated EELS results (**a**) Overview HAADF-STEM image of the structure along the [100] zone axis orientation, showing the presence of dark and light contrast layers in the structure (white and black arrows). The approximate region selected for STEM-EELS mapping is indicated by the white rectangle. (**b**) Atomic resolution EELS maps for Sr, Nb, Fe and Co, together with the simultaneously acquired ADF image. The color map displays the Co signal in green, and the Sr signal in red. No enrichment of the B cations can be seen at the light or dark contrast layers, confirming their random distribution throughout the structure. (**c**) Integrated EELS data ($22 \cdot 3$ pixel integration, raw data) from a light and dark layer, indicated by arrows in the ADF image in (**b**). No fine structure changes in the Fe $L_{2,3}$ or Co $L_{2,3}$ can be made out. (**d**) Bulk Fe $L_{2,3}$ edge acquired with excited monochromator ($\Delta E = 250$ meV). (**e**) Bulk Co $L_{2,3}$ edge acquired with excited monochromator.

$\sim$0.25 eV. Also, the edge onset value for Fe and Co was determined using the technique described in [19], as was 708.2 eV for Fe and 778.7 eV for Co. This bulk EELS data, corrected for the absolute edge onset is plotted in Fig. 3d, e. In the case of Fe, the edge onset value above 708 eV, together with fine structure comparison to standards proves the valency of iron to be very near to Fe^{4+} [19]. For Co, the onset value of 778.7 eV and fine structure signature points in the direction of Co^{3+}. With the cobalt valency being close to 3+ and the iron valency close to 4+, the oxygen defiency $\delta \approx 0.3$ can be estimated, being in close agreement with the experimentally measured $\delta = 0.28$ value. This anion deficiency in the $SrCo_{0.7}Fe_{0.2}Nb_{0.1}O_{2.72}$ structure is realised as an alternation of BO_2 and $BO_{1.4}$ layers.

In order to determine the crystal structure of ordered $SrCo_{0.7}Fe_{0.2}Nb_{0.1}O_{2.72}$, a refinement from PED data was performed. The relative intensities of diffraction peaks in PED data are more close to those from kinematical theory than in the case of SAED data, allowing them to be used for such refinement [21]. Reflections were extracted from a total of 8 PED patterns shown in Fig. 4. R_{symm} was calculated for every individual pattern with results ranging between 0.8% and 4.6%, well within acceptable limits. For each PED pattern an overlap between the zeroth order Laue zone reflections and reflections from higher order Laue zones was ruled out by simulating the PED patterns at 2.5° tilt using the program JEMS [22], therefore all zeroth order Laue zone reflections could be used in the refinement. The Friedel pair reflections were averaged and the geometrical correction factor (Lorentz factor) was applied, *i.e.* $C_{\mathrm{geom}} = g\sqrt{1-\left(\frac{g}{2R}\right)^2}$ where g is the reciprocal lattice vector, and R is the radius of the Laue circle [23]. The PED data treatment gave a total of 339 reflections with a resolution up until 0.6 Å. The coverage of reciprocal space until 1 Å resolution is 73%. The coverage between 1 Å and 0.6 Å however amounts only to 29%. A starting model was constructed based on two stacked perovskite unit cells, with random distribution of the B cations over both perovskite B–O layers and with one $BO_{1.4}$ layer (containing B1, O1) and one BO_2 layer (B2, O2), in accordance with the STEM-EELS and HAADF-STEM results. The data were entered in the Jana2006 program as consisting of three domains resulting from twinning by 120° rotations about the $\langle 221\rangle$ ($= \langle 111\rangle_p$) axes, as is consistent with the decrease of the symmetry from the space group of ideal perovskite $Pm\bar{3}m$ to $P4/mmm$. In the first step of the refinement, the scale factors of the 8 individual reflection files were determined. Next, the twin fraction and atomic parameters were refined, leading to a total of 14 refineable parameters. An attempt was made to refine the overall temperature factor, which produced the value of $U_{\mathrm{overall}} = -0.002(2)$ Å^2. The slightly negative value of U_{overall} can be attributed to the residual dynamic scattering impact into the intensities of high angle reflections. For the final refinement U_{overall} was fixed to 0. The refinement converged with a value $R_{\mathrm{all}} = 26.6\%$, which is reasonable for precession electron diffraction data. The final atomic parameters are shown in Table 1, the main interatomic dis-

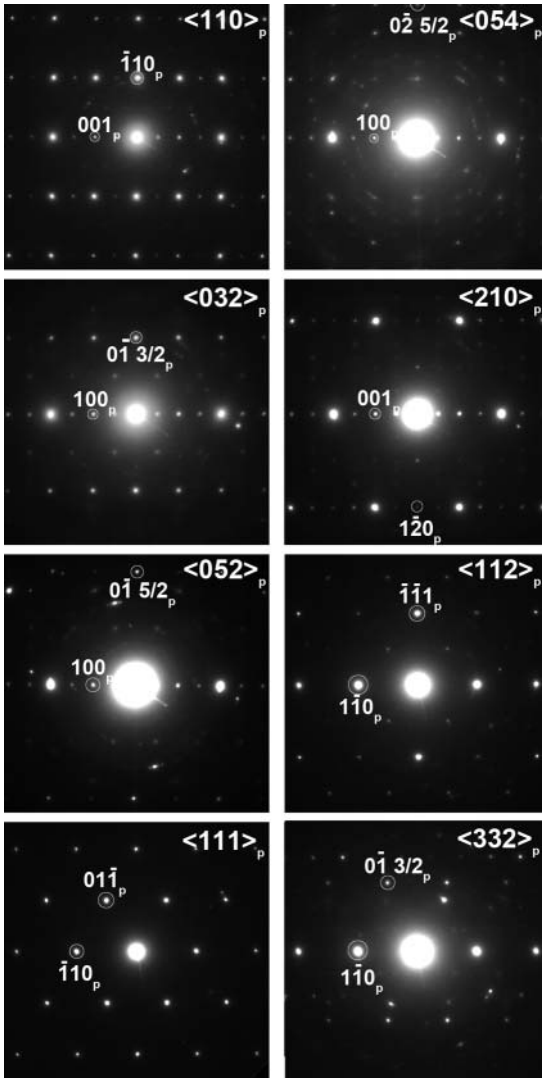

Fig. 4. PED patterns used for the refinement of the stucture from PED data. The patterns are indexed in the perovskite parent cell for clarity, to avoid multiple indices due to the twins that are present.

Table 1. Atomic parameters of $Sr_1Co_{0.7}Fe_{0.2}Nb_{0.1}O_{2.72}$.

Atom	Position	S.O.F.	*x/a*	*y/a*	*z/a*
Sr	2h	1	0.5	0.5	0.2618(14)
Fe1	1a	0.2	0	0	0
Co1	1a	0.7	0	0	0
Nb1	1a	0.1	0	0	0
Fe2	1b	0.2	0	0	0.5
Co2	1b	0.7	0	0	0.5
Nb2	1b	0.1	0	0	0.5
O1	4n	0.35	0.5	0.072(15)	0
O2	4i	0.5	0.5	0	0.466(3)
O3	8s	0.25	0.208(14)	0	0.245(8)

Table 2. Main interatomic distances (in Å) for $Sr_1Co_{0.7}Fe_{0.2}Nb_{0.1}O_{2.72}$.

Fe1Co1Nb1–O1	1.963(8)	Sr–O1	2.63(4)
Fe1Co1Nb1–O3	2.07(6)	Sr–O2	2.506(17)
Fe2Co2Nb2–O2	1.961(3)	Sr–O2	2.87(2)
Fe2Co2Nb2–O3	2.14(6)	Sr–O3	2.25(3)

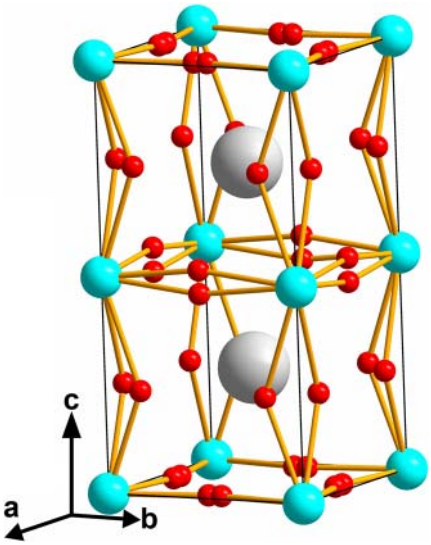

Fig. 5. Structure of $SrCo_{0.7}Fe_{0.2}Nb_{0.1}O_{2.72}$. Large white spheres represent the Sr site, small gray spheres the Co/Fe/Nb mixed site, darkest small spheres represent the oxygen sites.

tances are shown in Table 2. The refined structure is shown in Fig. 5. Since the oxygen vacancy and thus the $BO_2-BO_{1.4}$ layering was determined using STEM-EELS, no other vacancy model was tested.

The refined structure was used for the simulation of HAADF-STEM images. A simulated [100] HAADF-STEM image made at a thickness of 42.9 Å is shown in Fig. 6, placed in the close-up of an area of the HAADF-STEM image of Fig. 2. The simulated image agrees well with the experimental one.

To determine the influence of heating on this tetragonal structure, selected area electron diffraction patterns were also taken of the sample annealed at 600 °C in a dynamic vacuum of $P \sim 1.5\ 10^{-4}$ mbar. Although this annealing condition results in splitting the sample into two perovskite phases [11], the TEM investigation did not detect a second phase. The same type of layered oxygen-vacancy ordering is retained after the heat treatment and was detected for all studied crystallites. Perhaps, the two phases possess a slightly different oxygen content resulting in a small difference in their lattice parameters ($\sim$0.03 Å), which is hard to detect with SAED.

4. Discussion

Although the cubic perovskite structure was reported for $SrCo_{0.7}Fe_{0.2}Nb_{0.1}O_{2.72}$ using bulk diffraction techniques,

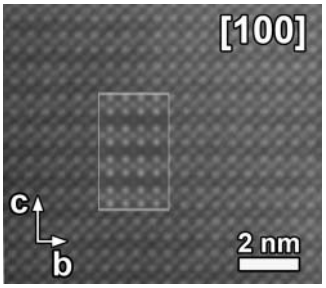

Fig. 6. HAADF-STEM image of $SrCo_{0.7}Fe_{0.2}Nb_{0.1}O_{2.72}$ with a calculated image indicated by a white border.

the situation appears to be drastically different when the structure is viewed at a local scale. At ambient conditions $SrCo_{0.7}Fe_{0.2}Nb_{0.1}O_{2.72}$ demonstrates a tetragonal $a_p \cdot a_p \cdot 2a_p$ superstructure with layered ordering of the oxygen atoms and vacancies: every second B–O layer becomes oxygen deficient. Strong positional disorder of the oxygen atoms was detected, obviously coupled to the random population of the B-positions by three sorts of cations with different crystal chemistry properties (Co^{3+}, $Fe^{\sim 4+}$ and Nb^{5+}). However, no superstructure reflections or splitting of the basic perovskite reflections due to the tetragonal distortion have been detected in earlier synchrotron X-ray powder diffraction studies. This apparent discrepancy is attributed to the pseudo-cubic nature of the structure (*i.e.* the closeness of the perovskite subcell parameters along the *a*, *b* and *c* tetragonal directions). This accounts for the absence of reflection-splitting, whereas heavy nano-scale twinning, associated with the pseudo-cubic structure, should lead to extreme broadening of the superlattice reflections, up to their apparent disappearance. However, the size of the coherently scattering domains is large enough to observe electron diffraction patterns of the ordered structure and to use the pseudo-kinematical intensities of the reflections measured in PED mode for structure refinement. It should be noted that local anion-vacancy ordering missed by X-ray or neutron diffraction techniques, but undubiously detected by TEM methods is quite common in perovskites [16, 17, 24–28].

Previous EXAFS experiments indicated that the Nb cations are octahedrally coordinated by oxygen, whereas the Co and Fe cations adopt a coordination number less than 6, implying that oxygen vacancies are located next to these cations [29]. Upon oxidation, the coordination numbers of Co and Fe increase. This is in agreement with our observation of random distribution of Co and Fe, so that both cations are present at the anion-deficient $BO_{1.4}$ layers. The coordination environment of Co was reported as being more distorted than the coordination environment of Fe and Nb. The difference in the geometry of the oxygen coordination of Co^{3+}, Fe^{4+} and Nb^{5+} is at the origin of the strong positional disorder of the oxygen atoms. The displacement of the O1 atom in the anion-deficient layer from its special $^1/_2$, 0, 0 position most probably reflects an average of tetrahedrally coordinated Co^{3+}, pentagonally and octahedrally coordinated Fe^{4+} and octahedrally coordinated Nb^{5+}. The displacement of O2 atoms above and below the mirror plane of the BO_2 layer and the shift of the O3 atoms away from the 4-fold symmetry axis can be interpreted as a result of cooperative tilting of the BO_6 octahedra. Considering the tolerance factor of $t = 1.008$ for the $SrCo_{0.7}Fe_{0.2}Nb_{0.1}O_{2.72}$ perovskite, it is hard to expect that the octahedral tilting is related to a mismatch between the A–O and B–O interatomic distances. Most probably this tilting compensates for the incomplete coordination environment of the Sr atoms due to the presence of the oxygen vacancies by shortening a fraction of the Sr–O3 and Sr–O2 interatomic distances. At the same time, it accounts for the displacement of the apical O3 atoms bridging an octahedron in the complete BO_2 layer with a tetrahedron in the anion-deficient layer, as it occurs, for example, in brownmillerites [30–33].

According to Podyacheva *et al.* [10], doping the $SrCo_{0.8-x}Fe_{0.2+x}O_{3-\delta}$ compound with Nb increases its stability against a transformation to the reduced brownmillerite phase, a transformation that is undesirable since oxygen-vacancy ordering decreases the oxygen permeation. Based on the structure determined in the current paper, this can now be explained by the fact that Nb^{5+} is present in the anion-deficient layer. Since Nb^{5+} strongly prefers the octahedral coordination, it prevents the formation of the brownmillerite phase, where the anion-deficient layers consist of infinite chains of BO_4 tetrahedra. Also the existence of twinned nanodomains in $SrCo_{0.7}Fe_{0.2}Nb_{0.1}O_{2.72}$ can prevent the formation of the brownmillerite phase, naturally limiting the space available for the propagation of the tetrahedral chains.

5. Conclusions

The "cubic" $SrCo_{0.7}Fe_{0.2}Nb_{0.1}O_{2.72}$ perovskite is demonstrated to adopt a tetragonal $a_p \cdot a_p \cdot 2a_p$ structure arising due to the ordered alternation of the perovskite BO_2 layers and anion-deficient $BO_{1.4}$ layers. The inclusion of the Nb^{5+} cations suppresses the formation of the brownmillerite phase in a reducing environment by demanding octahedral coordination around the Nb^{5+} cations and by the creation of nanotwinning which hinders the formation of continuous tetrahedral chains.

Acknowledgements. J. Hadermann and W. Dachraoui acknowledge financial support from the Research Foundation-Flanders (FWO G.0184.09N) and from the University of Antwerp through a BOF-NOI grant. This work was supported by funding from the European Research Council under the 7th Framework Program (FP7), ERC grant N∞246791 – COUNTATOMS. S. Van Rompaey, S. Lichtert and S. Turner thank the Flanders Science Fund (FWO) for funding as a Fellowship. The Qu-Ant-EM microscope was partly funded by the Hercules fund from the Flemish Governement.

References

[1] Teraoka, Y.; Zhang, H. M.; Furukawa, S.; Yamazoe, N.: Oxygen permeation through perovskite-type oxides. Chem. Lett. **11** (1985) 1743–1746.

[2] McIntosh, S.; Vente, J. F.; Haije, W. G.; Blank, D. H. A.; Bouwmeester, H. J. M.: Structure and oxygen stoichiometry of $SrCo_{0.8}Fe_{0.2}O_{3-d}$ and $Ba_{0.5}Sr_{0.5}Co_{0.8}Fe_{0.2}O_{3-d}$. Solid State Ionics **177** (2006) 1737–1742.

[3] Wang, Z.; Zhao, H.; Xu, N.; Shen, Y.; Ding, W.; Lu, X.; Li, F.: Electrical conductivity and structural stability of $SrCo_{1-x}Fe_xO_{3-\delta}$. J. Phys. Chem. Solids **72** (2011) 50–55.

[4] Sunarso, J.; Baumann, S.; Serra, J. M.; Meulenberg, W. A.; Liu, S.; Lin, Y. S.; da Costa, J. C. D.: Mixed ionic-electronic conducting (MIEC) ceramic-based membranes for oxygen separation. J. Membr. Sci. **320** (2008) 13–41.

[5] Kruidhof, H.; Bouwmeester, H. J. M; van Doorn, R. H. E.; Burggraaf, A. J.: Influence of order-disorder transitions on oxygen permeability through selected nonstoichiometric perovskite-type oxides. Solid State Ionics **63** (1993) 816–822.

[6] Qiu, L.; Lee, T. H.; Liu, L. M.; Yang, Y. L.; Jacobson, A. J.: Oxygen permeation studies of $SrCo_{0.8}Fe_{0.2}O_{3-\delta}$. Solid State Ionics **76** (1995) 321–329.

[7] Lu, H.; Son, S. H.; Kim, J. P.; Park, J. H.: A Fe/Nb co-doped $Sr(Co_{0.8}Fe_{0.1}Nb_{0.1})O_{3-\delta}$ perovskite oxide for air separation: Structural, sintering and oxygen permeating properties. Materials Letters **65** (2011) 702–704.

[8] Shao, Z.; Yang, W.; Cong, Y.; Dong, H.; Tong, J.; Xiong, G.: Investigation of the permeation behavior and stability of a $Ba_{0.5}Sr_{0.5}Co_{0.8}Fe_{0.2}O_{3-\delta}$ oxygen membrane. J. Membr. Sci. **172** (2000) 177–188.

[9] Shao, Z.; Dong, H.; Xiong, G.; Cong, Y; Yang, W.: Performance of a mixed-conducting ceramic membrane reactor with high oxygen permeability for methane conversion. J. Membr. Sci. **183** (2001) 181–192.

[10] Podyacheva, O. Y.; Ismagilov, Z. R.; Shmakov, A. N.; Iva-nov, M. G.; Nadeev, A. N.; Tsybulya, S. V.; Rogov, V. A.: Properties of Nb-doped $SrCo_{0.8}Fe_{0.2}O_{3-d}$ perovskites in oxidi-zing and reducing environments. Catal. Today **147** (2009) 270–274.

[11] Ivanov, M.; Shmakov, A.; Podyacheva, O.; Ismagilov, Z.: Structural aspects of oxygen stoichiometry in $SrCo_{0.6-x}Fe_{0.2}Nb_xO_{3-z}$ perovskites. Z. Kristallogr. Proc. **1** (2011) 313–318.

[12] Stevenson, J. W.; Amstrong, T. R.; Carneim, R. D.; Pederson, L. R.; Weber, W. J.: Electrochemical properties of mixed conducting perovskites $La_{1-x}M_xCo_{1-y}Fe_yO_{3-d}$ (M = Sr, Ba, Ca) J. Electrochem. Soc. **143** (1996) 2722–2729.

[13] Nadalin, R. J.; Brozda, W. B.: Chemical methods for the determination of the "oxidizing (or reducing) power" of certain materials containing a multivalent element in several oxidation states. Anal. Chim. Acta **28** (1963) 282–293.

[14] Petricek, V.; Dusek, M.: JANA2000: Programs for Modulated and Composite Crystals, Institute of Physics: Praha, 2000.

[15] Cristoph Koch, dissertation "Determination of core structure periodicity and point defect density along dislocations", April 2002

[16] Klie, R. F.; Browning, N. D.: Characterization of oxygen ordering in (La, Sr)FeO_{3-d} by atomic resolution *Z*-contrast imaging and electron energy-loss spectroscopy. J. Electron Microscopy **51** (2002) S59–S66.

[17] Ito, Y.; Klie, R. F.; Browning, N. D.; Mazanec, T. J.: Atomic resolution analysis of the defect chemistry and microdomain structure of brownmillerite-type strontium cobaltite. J. Am. Ceram. Soc. **85** (2002) 969–976.

[18] Egerton, R. F.: Electron Energy-Loss Spectroscopy in the Electron Microscope, 3rd ed. Springer 2011.

[19] Tan, H.; Verbeeck, J.; Abakumov, A.; Van Tendeloo, G.: Oxidation state and chemical shift investigation in transition metal oxides by EELS. Ultramicroscopy **116** (2012) 24–33.

[20] Turner, S.; Verbeeck, J.; Ramezanipour, F.; Greedan, J. J.; Van Tendeloo, G.; Botton, G. A.: Atomic Resolution Coordination Mapping in Ca_2FeCoO_5 Brownmillerite by Spatially Resolved Electron Energy-Loss Spectroscopy. Chemistry of Materials **24** (2012) 1904–1909.

[21] Vincent, R.; Midgley, P. A.: Double conical beam-rocking system for measurement of integrated electron diffraction intensities. Ultramicroscopy **53** (1994) 271–282.

[22] Stadelmann, P. A.: EMS – a software package for electron diffraction analysis and HREM image simulation in materials science. Ultramicroscopy **21** (1987) 131–145.

[23] Gemmi, M.; Nicolopoulos, S.: Structure solution with three-dimensional sets of precessed electron diffraction intensities. Ultramicroscopy **107** (2007) 483–494.

[24] Dachraoui, W.; Hadermann, J.; Abakumov, A. M.; Tsirlin, A. A.; Batuk, D.; Glazyrin, K.; McCammon, C.; Dubrovinsky, L.; Van Tendeloo, G.: Local Oxygen-Vacancy Ordering and Twinned Octahedral Tilting Pattern in the $Bi_{0.81}Pb_{0.19}FeO_{2.905}$ Cubic Perovskite. Chem. Mater. **24** (2012) 1378–1385.

[25] Abakumov, A. M.; D'Hondt, H.; Rossell, M. D.; Tsirlin, A. A.; Gutnikova, O.; Filimonov, D. S.; Schnelle, W.; Rosner, H.; Hadermann, J.; Van Tendeloo, G.; Antipov, E. V.: Coupled anion and cation ordering in $Sr_3RFe_4O_{10.5}$ (R = Y, Ho, Dy) anion-deficientperovskites. Journal of Solid State Chemistry **183** (2010) 2845–2854.

[26] D'Hondt, H.; Abakumov, A. M.; Hadermann, J.; Kalyuzhnaya, A. S.; Rozova, M. G.; Antipov, E. V.; Van Tendeloo, G.: Tetrahedral Chain Order in the $Sr_2Fe_2O_5$ Brownmillerite. Chem. Mater. **20** (2008) 7188–7194.

[27] Abakumov, A. M.; Alekseeva, A. M.; Rozova, M. G.; Antipov, E. V.; Lebedev, O. I.; Van Tendeloo, G.: Ordering of tetrahedral chains in the Sr_2MnGaO_5 brownmillerite. J. Solid State Chem. **174** (2003) 319–328.

[28] Hadermann, J.; Van Tendeloo, G.; Abakumov, A.: Transmission electron microscopy and structural phase transitions in anion-

deficient perovskite-based oxides. Acta Cryst. **A61** (2005) 77–92.

[29] Kriventsov, V. V.; Kochubey, D. I.; Ismagilov, Z. R.; Podyacheva, O. Yu.; Nemudry, A. P.: EXAFS Study of Nb Doped $Sr(Co/Fe)O_{3-x}$ Perovskites. Physica Scripta. **T115** (2005) 740–743.

[30] Abakumov, A. M.; Rozova, M. G.; Pavlyuk, B. Ph.; Lobanov, M. V.; Antipov, E. V.; Lebedev, O. I.; Van Tendeloo, G.; Sheptyakov, D. V.; Balagurov, A. M.; Bouree, F.: Synthesis and Crystal Structure of Novel Layered Manganese Oxide $Ca2MnGaO_{5+\delta}$. J. Solid State Chem. **158** (2001) 100–111.

[31] Abakumov, A. M.; Rozova, M. G.; Pavlyuk, B. Ph.; Lobanov, M. V.; Antipov, E. V.; Lebedev, O. I.; Van Tendeloo, G.; Ignatchik, O. L.; Ovtchenkov, E. A.; Koksharov, Yu. A.; Vasi'ev, A. N.: Synthesis, Crystal Structure, and Magnetic Properties of a Novel Layered Manganese Oxide $Sr_2MnGaO_{5+\delta}$. J. Solid State Chem. **160** (2001) 353–361.

[32] de la Calle, C.; Aguadero, A.; Alonso, J. A.; Fernandez-Diaz, M. T.: Correlation between reconstructive phase transitions and transport properties from $SrCoO_{2.5}$ brownmillerite: A neutron diffraction study. Solid State Sciences **10** (2008) 1924–1935.

[33] Battle, P. D.; Gibb, T. C.; Lightfoot, P.: The crystal and magnetic structures of Sr_2CoFeO_5. J. Solid State Chem. **76** (1988) 334–339.

[34] Hodges, J. P.; Short, S.; Jorgensen, J. D.; Xiong, X.; Dabrowski, B.; Mini, S. M.; Kimball, C. W.: Evolution of Oxygen-Vacancy Ordered Crystal Structures in the Perovskite Series $Sr_nFe_nO_{3n-1}$ ($n = 2$, 4, 8, and ∞), and the Relationship to Electronic and Magnetic Properties. J. Solid State Chem. **151** (2000) 190–209.